Surface & Coatings Technology xxx (xxxx) xxx–xxx

Contents lists available at ScienceDirect

Surface & Coatings Technology

journal homepage: www.elsevier.com/locate/surfcoat

Direct laser deposition cladding of $Al_xCoCrFeNi$ high entropy alloys on a high-temperature stainless steel

Qi Chao[a,*], Tingting Guo[a], Tom Jarvis[b], Xinhua Wu[b], Peter Hodgson[a], Daniel Fabijanic[a,*]

[a] Institute for Frontier Materials, Deakin University, Geelong, VIC 3216, Australia
[b] Monash Centre for Additive Manufacturing, Monash University, Clayton, VIC 3800, Australia

ARTICLE INFO

Keywords:
Direct laser deposition
High entropy alloy
Dilution
Coating
Laser cladding
Thermal stability

ABSTRACT

$Al_xCoCrFeNi$ (x = 0.3, 0.6 and 0.85) high entropy alloy (HEA) claddings were produced by coaxial direct laser deposition (DLD) on a 253MA austenitic steel substrate using a mixture of blended elemental powders. The effect of key processing variables on the formation of HEA claddings and the compositional mixing between the deposited layer and the substrate was investigated through a three-level parametric study on laser power, laser scanning speed, laser beam size, powder feeding rate and hatch distance. Using selected parameters, HEA claddings mostly free of defects were successfully manufactured with very minimal dilution. With an increase in the Al mole fraction from 0.3 to 0.6 and 0.85, the HEA claddings displayed an evolution of crystal structure from FCC, to FCC + BCC and BCC, accompanied by an increase in microhardness. The increased Al content also resulted in reduced microstructural stability of the coatings and hence higher level of thermal softening upon isothermal treatment at 1000 °C.

1. Introduction

High entropy alloys (HEAs) are a relatively new class of alloy system comprising of 4–5 principle alloying elements at a concentration between 5 and 35 at.% [1–5]. Contrary to conventional phase rule prediction, many HEA compositions form simple solid solutions instead of brittle intermetallic compounds [3–6]. HEAs possess many attractive properties such as high strength [3–5], excellent wear [7], corrosion [8] and thermal softening resistance [9], thermally stable microstructure [10–12], low inter-diffusion [13], and high oxidation resistance [14–17]. Therefore, HEAs are gaining interest as protective coatings for engineering alloys in critical applications.

HEA coatings have been produced on a metal surface by various techniques including welding [18], physical vapour deposition [19], thermal spraying [20], and laser cladding [14,21–33]. Focussing on laser HEA cladding fabrication, the vast majority of prior studies have used a static powder bed technique [14,21–27,33]. Here a layer of pre-alloyed or mixed power is placed on the substrate surface and scanned by a laser beam, which melts the powder and partially melts the substrate to create an alloy cladding with a metallurgical bond to the substrate. Studies of this process include successful formation of various HEAs on steels [23–27,33], copper [28,29], aluminum [30], magnesium [31] and titanium alloy [14] substrates, where the cladding displayed improved wear and corrosion performances relative to the substrate. A clear practical limitation of this process is the ability to treat only flat and horizontal surfaces. In contrast, direct laser deposition (DLD) is a technique where the powder is inert gas transported and melted by a focused laser attached to a multi-axis head, and is routinely used to additively manufacture complex geometry metallic parts or to discrete area clad/repair of components [34]. Despite the clear advantages of this “blown powder” laser deposition technique its use in HEA cladding is rare [31,32].

Motivated to improve wear and corrosion resistance, Yue et al. [31] have reported an attempt to clad a magnesium substrate with an AlCoCrCuFeNi HEA by a direct blown powder cladding technique. The choice of substrate, with its boiling temperature below the HEA melting point, created difficulty and required a complex processing route. Also, severe intermixing between the substrate and deposit (i.e. dilution) occurred, wherein only the top 50 μm of a total coating thickness of 200–300 μm had an approximate HEA composition. One further study by Ocelík et al. [32] used a blown powder technique to fabricate AlCoCrFeNi and AlCrFeNiTa HEA claddings on an AISI 305 stainless steel plate. A blended mixture of elemental powders was used, which offers process convenience, however this resulted in some unmelted tantalum powder due to a very high melting point. Additionally, a strong dilution effect (mainly Fe from the substrate) was experienced which required three successive ~600 μm layer depositions to finally achieve the desired HEA composition in the outer layer. It is worth noting that both

* Corresponding authors.
E-mail addresses: qi.chao@deakin.edu.au (Q. Chao), daniel.fabijanic@deakin.edu.au (D. Fabijanic).

http://dx.doi.org/10.1016/j.surfcoat.2017.09.072
Received 23 May 2017; Received in revised form 12 September 2017; Accepted 20 September 2017

Table 1
Processing parameters and cladding metrics of I) single track deposition, II) square deposition trials on $Al_{0.3}CoCrFeNi$ and III) $Al_xCoCrFeNi$ coatings.

Trial number		Laser power P (W)	Scanning velocity S (mm/min)	Laser beam diameter D (mm)	Powder feed rate F (g/min)	Hatch distance H (mm)	Laser track width W (mm)	Build-up height T_C (μm)	Penetration depth T_P (μm)	Interface thickness T_D (μm)	Dilution F_D (%)	Powder efficiency P_E (%)	Energy density E_S (J·mm^{-2})
I	I-a. Pre-scan	800	800	3	/	/	1.36 ± 0.1	0	68	/	/	/	25.5
	I-b. Baseline	1000	800	3	F = ~13.6	/	1.9 ± 0.02	491 ± 32	110 ± 10	10.3 ± 1.6	12.5	30.1	31.8
	I-c	800	800	3	F	/	1.1 ± 0.11	261 ± 0.18	45 ± 0.8	7.75 ± 1.1	11.3	9.3	25.5
	I-d	1200	800	3	F	/	2.13 ± 0.03	554 ± 28	162 ± 0	13.75 ± 3.9	17.3	38.1	38.2
	I-e	1000	400	3	F	/	1.92 ± 0.01	639 ± 18	158 ± 12	22.5 ± 4.5	14.6	20.5	63.7
	I-f	1000	1200	3	F	/	1.17 ± 0.04	167 ± 16	54 ± 14	7.5 ± 1.4	19.5	9.1	21.2
	I-g	1000	800	2	F	/	1.86 ± 0.04	500 ± 34	194 ± 16	14.75 ± 2.1	21.6	30.2	47.8
	I-h	1000	800	4	F	/	0.8 ± 0.03	36 ± 4	59 ± 4	/	/	0.9	23.9
	I-i	1000	800	3	0.5F	/	1.74 ± 0.02	207 ± 24	119 ± 6	22.5 ± 1.4	29.9	22.4	31.8
	I-j	1000	800	3	1.5F	/	1.59 ± 0.04	550 ± 40	45 ± 5	7.3 ± 1.6	5.3	19.5	31.8
II	II-a	1000	800	3	F	0.75	/	932 ± 17	176 ± 7	24 ± 5.6	8.6	32.9	90.3[a]
	II-b	1000	800	3	F	1	/	816 ± 7	192 ± 8	21.5 ± 5.1	10.5	38.4	74.4[a]
	II-c	1000	800	3	F	1.5	/	604 ± 7	196 ± 7	20.5 ± 3.6	14	42.7	62.5[a]
III	$Al_xCoCrFeNi$	1000	800	2	F	1	/	845 ± 7	108 ± 3	30.9 ± 4.2	9.1	39.8	78.7[a]

[a] The energy density per unit of deposition volume ($E_V = P / (S{\cdot}T{\cdot}H)$, in J·mm^{-3}) is used, where $T = T_C + T_P$.

these prior studies were performed by the side-cladding variant of blown powder DLD.

Here powder is delivered using a lateral/side powder feeder nozzle, which can cause variation in cladding characteristics (e.g. “against hill” or “over hill” cladding) depending on the relative motion of the laser head to the powder stream [34]. There have been no reported studies on HEA claddings by coaxial DLD, where the powder is delivered coaxially with the laser beam, and thus free from geometric constraints. Although there are notable first attempts at blown powder laser deposited HEA claddings, to advance the field there is a need for a systematic parametric approach and a detailed microstructural undertaking to address the critical issues encountered by this technology including dilution, compositional inhomogeneity, powder efficiency etc.

In the present study, the $Al_xCoCrFeNi$ (x = 0.3, 0.6 and 0.85) HEA system was chosen for coaxial DLD claddings from elemental powders on a 253MA high-temperature stainless steel substrate. It is well established in near-equilibrium cast HEAs that increasing Al content in this alloy system results in a transformation from face centred cubic (FCC) to body centred cubic (BCC) solid solution crystal structures [10,35]. In DLD processing, whether this HEA system holds its phase stability is of interest, considering possible dilution of HEA claddings and the rapid solidification rate (10^3–10^6 K/s), large thermal gradients (10^5–10^7 K/m) [36,37] and complex local thermal history between successive deposits during laser cladding. Herein, a systematic development path was taken including a 3-level 4-parameter study on single track deposits firstly performed to establish process conditions that optimise the deposit shape and minimise the dilution between coating and substrate. After that, multiple-track claddings were produced for all HEA compositions and extensively characterized for phase content, micro/macro-structure, crystallographic texture and chemical homogeneity. As a main target application of these coatings is to protect substrate alloys in high temperature oxidizing environments, the impact of thermal exposure (i.e. 1000°C for up to 100 h) on the deposit microstructure and properties (micro-hardness) was also examined.

2. Experimental procedure

In this study, the $Al_xCoCrFeNi$ (x = 0.3, 0.6 and 0.85 in atomic ratio) HEA coatings were produced by direct laser deposition on a 16 mm thick 253MA austenitic steel plate with an average grain size of ~40 μm in the hot-rolled and annealed condition. This steel has a composition of C0.03Cr24.0Ni14.3Si1.6Mn0.05 (wt%, Fe balance), which is specially designed mainly for high temperature applications up to 1150°C in oxidizing atmospheres [38]. The substrate plate was machined flat, sand blasted to reduce laser reflectivity and cleaned with acetone prior to deposition.

Direct laser deposition was performed using a TRUMPF TruLaser Cell 7040 coaxial blown powder laser deposition facility equipped with a twin powder feeder and a 1030 nm wavelength 4 kW TruDisk 4001 disc CO_2 laser. Herein, the $Al_xCoCrFeNi$ HEA claddings were fabricated from spherical gas-atomized Al, Co, Cr, Fe and Ni (~99.9–99.99% purity) powders in the size range of 50–150 μm provided by TLS, Germany and Micronmetals, USA. To avoid settling and segregation by density, the higher density element powders (Co, Cr, Fe and Ni) were firstly blended using a rotary tumbler for ~12 h. After that, the premixed CoCrFeNi powder and Al powder were loaded in separate hoppers and independently transported by a 99.999% ultra-high purity helium carrier gas to the focused laser on a 5-axis controllable head at carefully calibrated mass flow rates. The deposition region was sealed during cladding and continuously purged with high purity argon gas to maintain a relatively low oxygen atmosphere (< 20 ppm).

A single-track deposition parametric study of $Al_{0.3}CoCrFeNi$ was initially carried out to study the effect of key processing parameters on the deposit geometry and the extent of interface mixing. A pre-scan trial was first performed without powder flow rate to simulate a practical DLD operation with laser preheating of the substrate (Trial I.a, Table 1). This was followed by a matrix of experiments consisting of three levels of laser power (P), laser scanning speed (S), laser beam diameter (D) and powder mass feed rate (F) (Trials I.b–j, Table 1). After that, single layer squares (~20 × 20 mm) of $Al_{0.3}CoCrFeNi$ claddings were produced with varying hatch distance (H = 0.75, 1 and 1.5 mm, Trials II.a–c, Table 1) and the established parameters (Full trials III, Table 1) were applied to produce $Al_xCoCrFeNi$ (x = 0.3, 0.6 and 0.85) single layer claddings (hereafter referred to as $Al_{0.3}$, $Al_{0.6}$ and $Al_{0.85}$ HEA, respectively) with the dimensions of ~20 × 80 mm. All the depositions were produced at the focal working distance of 16 mm and by a building sequence of parallel vectors across the shorter dimension. $Al_xCoCrFeNi$ (x = 0.3, 0.6 and 0.85) claddings were polished flat by removing the top ~200 μm surface layer and then subjected to isothermal holding at 1000 °C for up to 100 h in air to assess the thermal stability of the HEA clad microstructures.

Phase determination was conducted on polished surfaces of the HEA claddings (~200 μm removed) using a laboratory PANalytical PRO MRD (XL) X-ray diffractometer with Cu Kα radiation in point focus. Microstructural characterization was performed on cladding cross-sections using optical microscopy (OM) and scanning electron microscopy (SEM), including backscattered electron (BED) imaging, electron backscattered diffraction (EBSD) and energy-dispersive X-ray spectroscopy (EDS). The samples for SEM, XRD analysis and hardness

measurement were prepared following a standard grinding/polishing procedure including final polishing with a 0.04 μm colloidal silica suspension (OPS, Struers, Denmark). SEM analysis was performed using a JEOL JSM 7800F field emission gun SEM (FEG-SEM) operated at 20 kV. EBSD and EDS or combined analysis was conducted using an automated AZtecHKL software (Oxford Instruments).

Microhardness measurement was performed using a UMIS ultra-micro indentation system equipped with a Berkovich-type diamond indenter. A sequence of up to 60 indents were measured through the cladding cross-section with a maximum load of 30 mN and a minimum separation distance of ~20 μm. Tests were performed under closed loop control at a loading rate of 1.5 mN/s and the hardness was calculated from the indentation depth and a calibrated area function of the indenter. Three profiles were measured for each HEA cladding before and after annealing at 1000°C.

3. Results

3.1. Parametric study

3.1.1. Single track HEA deposition

An example cross-sectional microstructure of a single-track $Al_{0.3}CoCrFeNi$ deposition on 253MA (Trial I.b, Table 1) is shown in Fig. 1a, consisting of an approximately hemispherical melt deposit above the substrate surface (buildup/clad layer, thickness T_C) and a melt zone below the substrate surface (laser penetration layer, depth T_P). Beneath the melt deposit there is an interface region (inter-diffusion layer, width T_D) with an intermediate composition between the clad and the substrate as a result of their intermixing (i.e. dilution). SEM-EDS line scan on the deposit centreline revealed the composition of the melt deposit, which for Trial I.b is generally close to the calculated $Al_{0.3}CoCrFeNi$ HEA composition (Fig. 1b). However, the cladding composition was inhomogeneous through the clad, consisting of unmelted powders (Fe particle in Fig. 1b, though more commonly Cr) and porosity/inclusions, commonly observed in all single track deposit trials. The inter-diffusion layer was ~8 μm in thickness, representing a quite steep compositional change from the substrate to the HEA clad (Fig. 1b). Apart from this region, the $Al_{0.3}$ HEA and 253MA alloy compositions were largely reserved on each side, indicative of a relatively small extent of dilution.

In laser claddings, dilution (F_D) is defined as the percentage of the total volume of the surface layer contributed by the melting of the substrate [39]. It can be calculated by assessment of the clad cross-section;

$$F_D = A_P/(A_C + A_P) \quad (1)$$

where A_C and A_P are the cross-sectional area of the clad and penetration layers, respectively (Fig. 1a). Herein, the clad area A_C and penetration area A_P are calculated using the clad height (T_C), penetration depth (T_P) and clad width (W), assuming the clad cross-section lies on a circle and the melt zone has a triangular shape (Fig. 1a) [34]. Also, the conversion of powder feedstock to cladding (powder efficiency, P_E) can be calculated using the clad area A_C, powder feeding rate F, scanning speed S and powder density ρ_P [34];

$$P_E = A_C S \rho_P / F \quad (2)$$

By varying the processing parameters for single-track depositions, the dimensional characteristics of melt pool profile and degree of dilution were strongly affected. Cross-sectional images of all resultant claddings from Trials I.a–j (Table 1) are shown in Fig. 2a–j. Key metrics from cladding analysis (T_C, T_P, T_D, F_D, P_E) are summarized in Table 1 and plotted against key process parameters (P, S, D and F) in Fig. 3a–d. The broad aims of this work include identifying process parameters that produce a balance between efficient deposition (high T_C, W and P_E) and minimal dilution (T_D, T_P and F_D).

Prior to deposition, the substrate was pre-scanned by a single laser

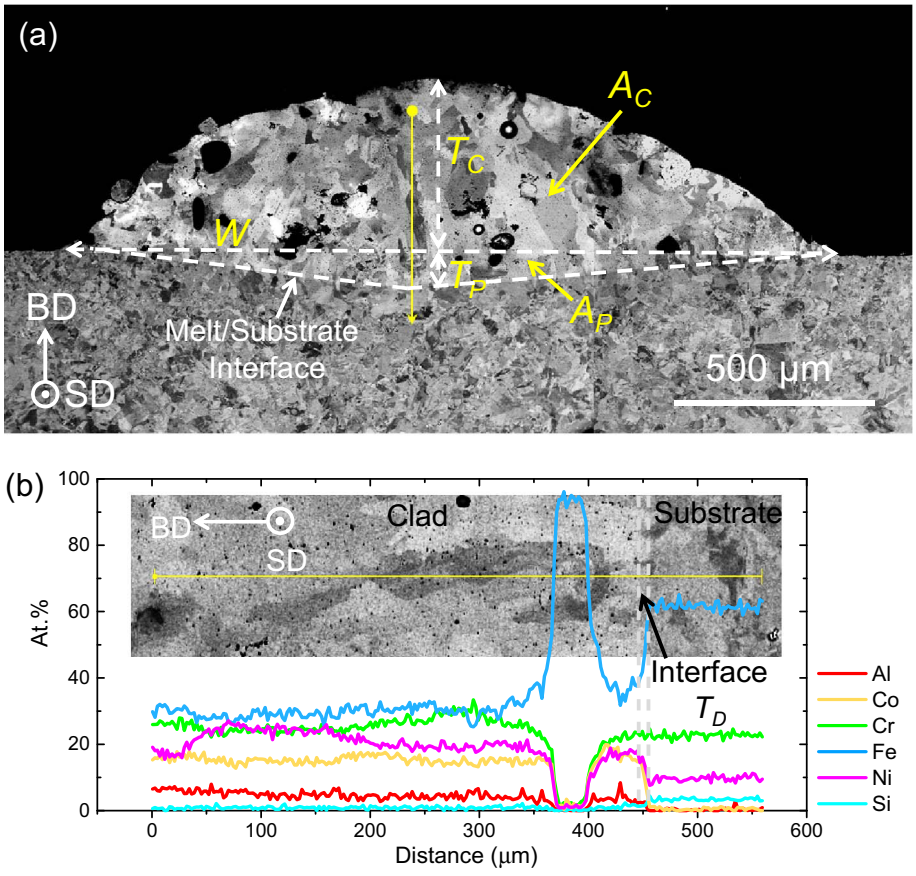

Fig. 1. a) Cross-sectional SEM-BED image of a typical single-track deposition (baseline condition) of $Al_{0.3}CoCrFeNi$ coating on 253MA alloy and b) EDS line scan profile through the coating interface. BD = Build Direction, SD = Laser Scan Direction.

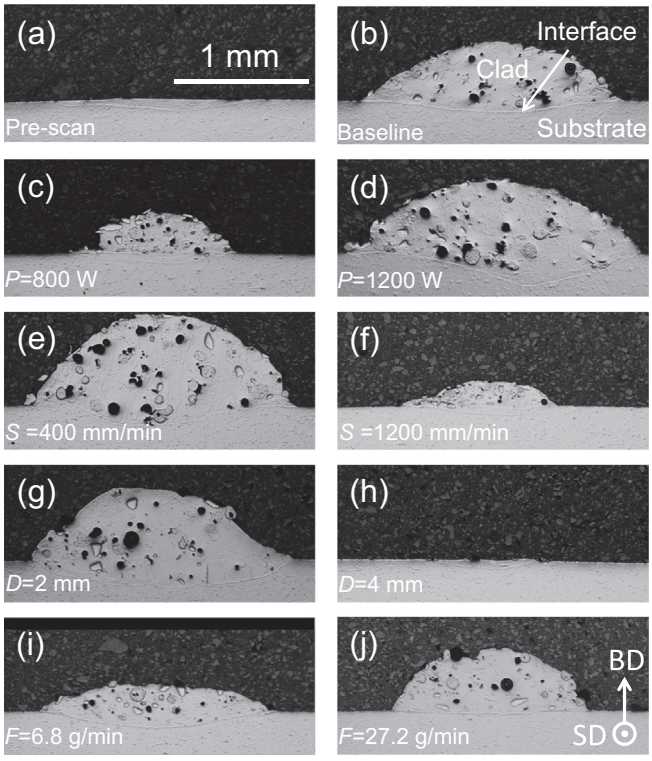

Fig. 2. Cross-section images of the $Al_{0.3}CoCrFeNi$ single-track depositions manufactured using different parameters: a) pre-scan condition and b) baseline condition using P = 1000 W, S = 800 mm/min, D = 3 mm and F = 13.6 g/min. The processing parameters same as the baseline condition are not listed in c–j).

vector without powder feeding (see Table 1 for process conditions and resulting microstructure in Fig. 2a). This produced a ~1.36 mm wide melt zone with a penetration depth of ~68 μm into the substrate. After deposition using the baseline parameters, a ~1.9 mm wide single track was produced with an average clad height of ~491 ± 32 μm and a mean laser penetration depth of ~110 ± 10 μm (Fig. 2b). Some general trends emerged from subsequent Trials I.c–j. An increase in laser power from 800 W to 1200 W led to an increase in clad width (W), clad height (T_C), penetration depth (T_P), and inter-diffusion thickness (T_D) (Fig. 3a). In contrast these clad metrics generally decreased with an increase in laser beam diameter (D, Fig. 3b) and laser scanning speed (S, Fig. 3c). Specifically, the deposition width was almost constant at ~1.9 mm from S = 400 to 800 mm/min and from D = 2 to 3 mm. In other words, a clad width close to the laser beam diameter was produced at D = 2 mm when other parameters were fixed to the baseline condition. Beyond that, the deposition width became much smaller than the laser beam size and the additive elemental powders were hardly deposited at D = 4 mm (Figs. 2h and 3c). Increasing the powder feed rate F had a moderate effect on decreasing inter-diffusion thickness T_D, laser penetration depth T_P and increasing the clad thickness (T_C) while the clad width W was not significantly affected (Figs. 2i–j and 3d).

Corresponding to the geometrical variation at different processing conditions, the single-track depositions revealed different extents of dilution (~5.3–30%) and powder efficiency (0.9–38%). The evolution of dilution (F_D) was mostly consistent with the inter-diffusion thickness T_D, except for Trials. I.e–f (Figs. 2e–f and 3b), where a combination of different parameters including laser-material interaction time (D/S), combined powder feeding rate (F/S) and energy density were simultaneously affected by varying laser scanning speed S. The correlations between the cladding characters (e.g. dilution, powder efficiency) and processing condition (e.g. energy density) are rather complex and

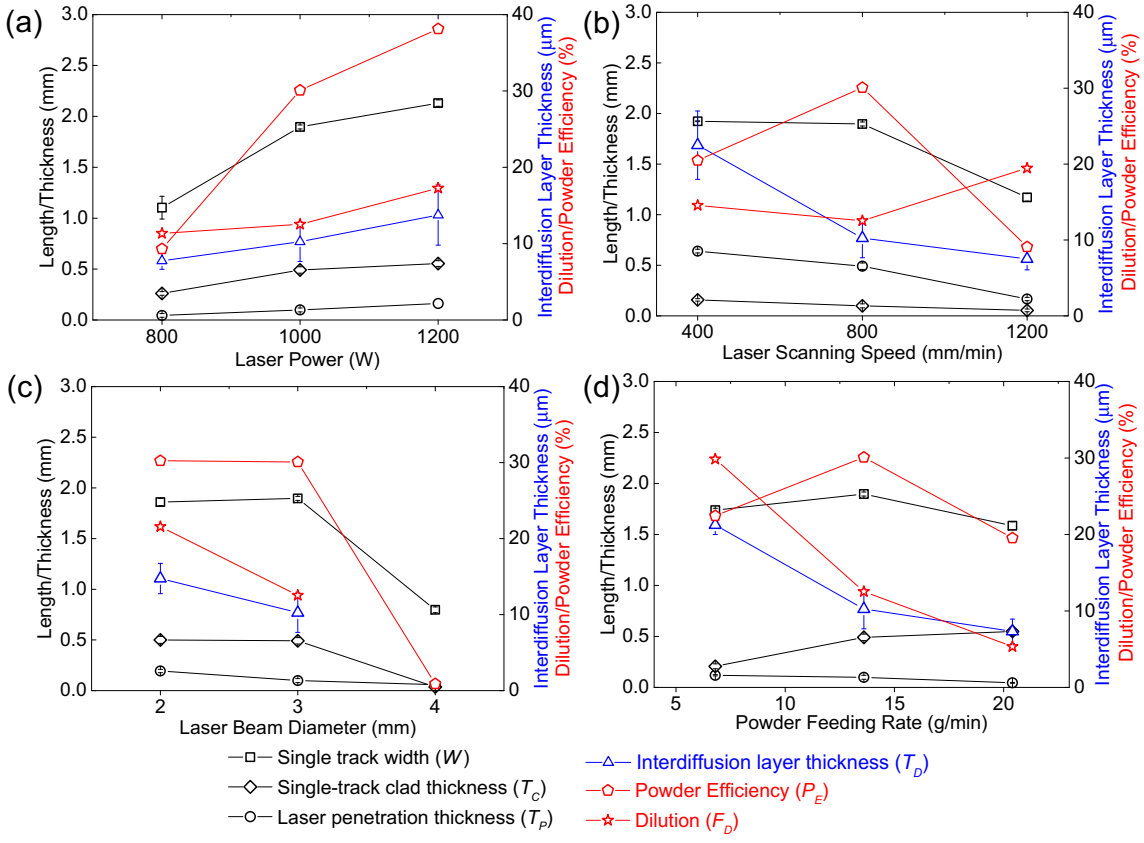

Fig. 3. The clad metrics of $Al_{0.3}CoCrFeNi$ single laser depositions as a function of different processing variables: a) laser power P, b) laser scanning speed S, c) laser beam diameter D and d) powder mass feeding rate F.

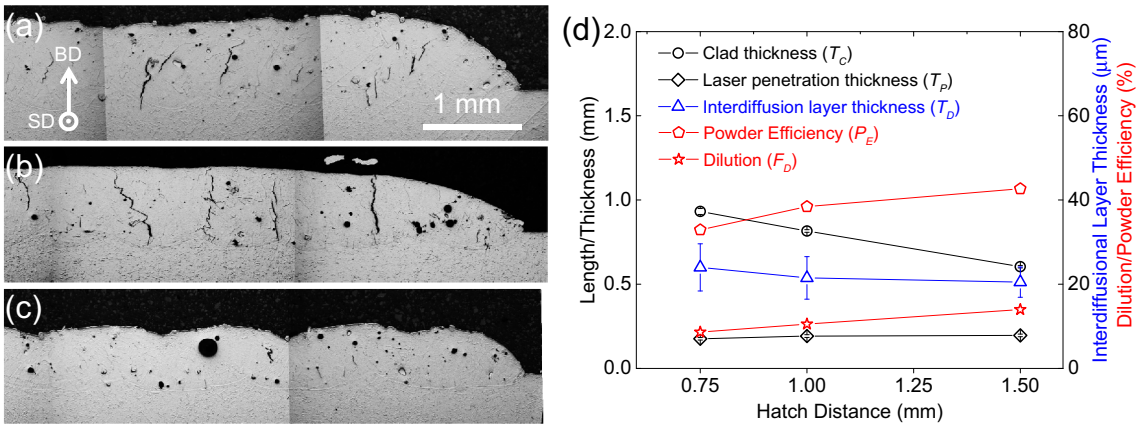

Fig. 4. a–c) Cross-sectional images and d) clad metrics of $Al_{0.3}CoCrFeNi$ single layer depositions with different hatch distances: a) H = 0.75 mm, b) H = 1 mm and c) H = 1.5 mm.

will be discussed later. Here it appeared a combination of processing parameters including P = 1000–1200 W, S = 800 mm/min, D = 2–3 mm and F = 13.6 g/min may provide a reasonable balance between cladding efficiency (e.g. ≥30%) and controlled dilution ($F_D \leq 20\%$ and $T_d \leq 15$ μm), which can also be used in multiple-track deposition.

3.1.2. Multiple-track single layer HEA deposition

Claddings (20 × 20 mm) of $Al_{0.3}CoCrFeNi$ single-layer coatings were manufactured with differing hatch distances (H) of 0.75 mm, 1 mm and 1.5 mm using the baseline parameters, representing an overlap ratio ($OR = 1 - H / W$, W = 1.9 mm) of 60, 47 and 21%, respectively (Fig. 4a–c). As a result of re-melting during successive depositions, the population of un-melted particles and porosity/inclusion was significantly reduced, when compared to the single-track deposits (Figs. 2 and 4a). However, vertical cracks were frequently found in the claddings, especially for the relatively small hatch distances of 0.75 and 1 mm (Figs. 4a, b). This is perhaps due to the use of a laser beam size much greater than the clad width, which may cause undesirable hot cracking during successive single layer deposition. For H = 1.5 mm, the clad surface was distinctly wavy (Fig. 4c), resulting in a highly variable clad thickness, mainly due to an unsuitable overlap ratio (21%) [40]. With increasing hatch distance, the clad height (T_C) and inter-diffusion thickness (T_D) decreased as less volume of elemental powder is fed to the deposition region for a given area of substrate surface. In comparison, the laser penetration depth (T_P) seems unaffected, maintaining a constant thickness of ~190 μm for all hatch distances (Fig. 4d). Compared with the baseline single-track deposit, the powder efficiency and extent of dilution were slightly higher in the claddings, which surged with an increase in hatch distance. To progress to full cladding trials of various HEAs, a laser beam diameter of 2 mm was chosen ($W \approx D$) with an overlap ratio of ~50% to produce claddings with uniform thickness.

3.2. Microstructure and properties of HEA claddings

3.2.1. As-deposited HEA microstructures

$Al_xCoCrFeNi$ coatings with varying Al contents (i.e. x = 0.3, 0.6 and 0.85) were produced by DLD on the 253MA alloy using the established process parameters (Full trials III, Table 1), and the resulting cross-sectional microstructures are shown at various scales in Fig. 5. EDS analysis (Fig. 6) revealed that the cladding thickness was ~900 μm for all HEAs, and that the elemental composition was quite uniform across the thickness and very close to the designed atomic ratio of the HEAs (refer to averaged EDS line scan atomic concentrations in Table 2). In all HEA claddings, the Fe mole fraction was slightly higher than other elements whereas the Ni ratio was comparatively lower, mostly likely due to dilution from the Fe-rich Ni-lean 253 alloy substrate (Table 2). The inter-diffusion zone was increased in thickness relative to single track depositions (~30.9 ± 4.2 μm for all cladding compositions), presumably due to successive re-melting. This T_D value is still much lower than that of many other HEA claddings produced by blown powder or powder bed laser deposition routes from prior studies (typically in hundreds of microns [30–32,41]).

The variation of Al content (i.e. x = 0.3, 0.6 and 0.85) resulted in different phase constitutions in the HEA claddings (see XRD analysis in Fig. 7a and EBSD phase maps in Fig. 8): principally FCC phase for x = 0.3, mixed FCC + BCC phases for x = 0.6 and BCC phase for x = 0.85. The as-deposited claddings were mostly crack-free for the $Al_{0.3}$ and $Al_{0.6}$ compositions, whereas some minor vertical cracks were observed in the $Al_{0.85}$ cladding, most likely due to the formation of brittle Al-rich BCC phase (Figs. 5–9) [3]. The cladding cross-section was composed of coarse columnar grains, mostly enclosed by high angle grain boundaries (HAGBs), and the mean grain size was ~40.9 ± 3.7, 38.2 ± 3.1 (FCC grain size) and 32.5 ± 1.5 μm for the $Al_{0.3}$, $Al_{0.6}$ and $Al_{0.85}$ HEA claddings, respectively. The columnar grains are commonly orientated towards the build-up direction (BD), while small proportion of fine equiaxed grains were locally observed near the cladding surface. It is worth noting that a quite random crystallographic texture is characteristic of all the HEA claddings (EBSD IPF maps in Fig. 8), which is distinct from the single phase $Al_{0.3}$ and $Al_{0.85}$ HEA bulk columns produced by DLD in an earlier work, representing a strong 〈001〉 fiber texture along the solidification direction (i.e. BD) [35].

Detailed microstructural observation revealed a uniform cellular sub-structural network with an average size of ~5.7 μm in the grain interiors of the $Al_{0.3}$ HEA (Fig. 5c). SEM-EDS mapping represented a relatively homogenous distribution of all principle elements throughout the FCC grain boundaries and cellular networks (Fig. 9a and associated EDS maps). The cellular structure could be dislocation tangles [42] formed due to directional thermal straining during rapid solidification or micro-segregation, akin to the non-equilibrium solidification behavior and resultant submicron cellular networks formed in a selective laser melted austenitic 316 L stainless steel [43]. With an increase of the Al mole ratio from 0.3 to 0.6, a small fraction of intercellular BCC phase was observed in the FCC matrix due to the solidification segregation of Al and Ni (Figs. 8d and 9b) [35]. For the $Al_{0.85}$ cladding, detailed backscattered electron imaging revealed local bright atomic contrast (Z contrast) at some BCC grain boundaries (Figs. 5i and 9c). A similar grain morphology was observed in powder-bed laser surface alloying of a BCC AlCoCrFeNi coating on a 304 SS substrate [23] and also in bulk columns of DLD BCC $Al_{0.85}CoCrFeNi$ [35], with the latter suggesting a grain boundary segregation of Cr and Fe. However, the SEM-based EDS mapping did not reveal any local grain boundary compositional variation, most likely due to an incompatible spatial resolution of the SEM-EDS analysis. Noticeably, a dispersion of spherical sub-micron inclusions rich in Al and O was present throughout the microstructures of all HEAs claddings (Figs. 5 and 9). These are

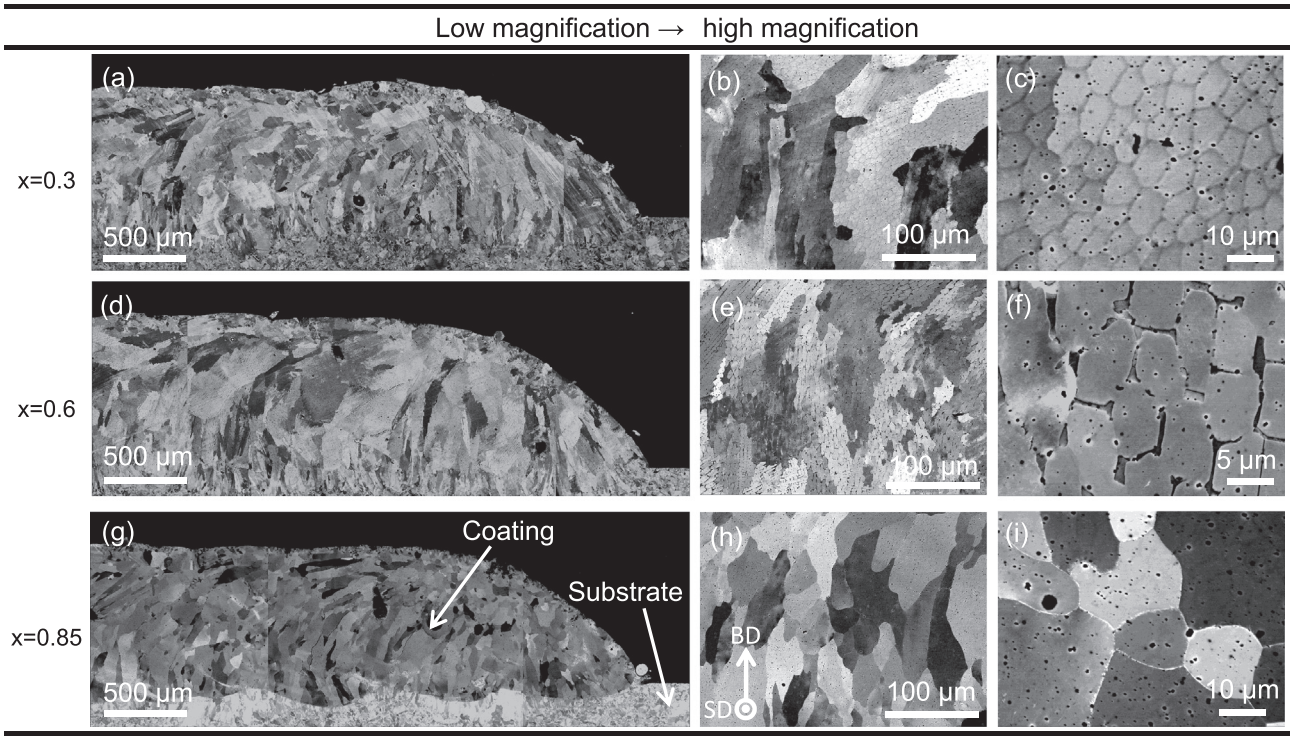

Fig. 5. Cross-sectional SEM micrographs of the $Al_xCoCrFeNi$ single layer depositions at different magnifications: a–c) $x = 0.3$, d–f) $x = 0.6$, g–i) $x = 0.85$.

aluminum oxide particles formed during melting, where the oxygen source is likely a combination of natural oxides on the elemental powders and deposition substrate or from the process atmosphere [43].

3.2.2. Thermal stability

After isothermal holding at 1000 °C for 100 h, the microstructure in the $Al_{0.3}$ HEA cladding was largely unaltered apart from the disappearance of the cellular sub-structural networks, wherein the single FCC phase composition and grain morphology was mostly retained (Figs. 7b, 11a, b and 12a including associated EDS maps). The $Al_{0.6}$ HEA experienced moderate phase separation and a change in the BCC phase morphology from intercellular-dendrites to larger discrete phases (Figs. 11c,d and 12b). XRD analysis revealed the appearance of ordered BCC phase (B2) with a very minor (100) peak (Fig. 7b). This suggests that some BCC phase enriched by Al and Ni elements (Fig. 12c) has transformed into B2 phase, as reported in [44]. Additionally, ~1–2 μm sized particles enriched in Cr, Mn and C (likely to be $M_{23}C_6$ type alloy carbides) formed, presumably due to the dilution of C and Mn from the substrate. The most significant microstructural changes were observed in the $Al_{0.85}$ HEA coating (Figs. 11e, f and 12c), mainly due to the transformation from BCC to FCC and B2 phases as reported in earlier studies [10,12]. A FCC-BCC dual phase microstructure was found after isothermal holding, consisting of grain boundary precipitation and transformed FCC phase throughout the grain interior. It should be noted that no remarkable coarsening in as deposited columnar FCC/BCC grains or Al-O-rich oxide particles was observed through isothermal holding treatment at 1000 °C for 100 h, perhaps due to their inherent stability.

3.2.3. Mechanical behavior evolution

Micro-hardness measurements through the cross-section of as-deposited claddings showed that the $Al_{0.3}$ HEA has a micro-hardness of ~2.3 GPa, slightly lower than that of the 253MA substrate (~2.5 GPa, Fig. 10a). This is consistent with the tensile yield strength reported elsewhere (i.e. 175–300 MPa for $Al_{0.3}$ HEA [3,45] and ~310 MPa for 253MA [38]). The hardness of the $Al_{0.6}$ cladding fluctuated due to the presence of the hard BCC phase in a softer FCC matrix whereas the average hardness was slightly higher than the $Al_{0.3}$ cladding and substrate. The single BCC phase $Al_{0.85}$ cladding displayed a constant micro-hardness of ~6 GPa throughout the thickness. The higher hardness in the BCC HEA results from the heavy lattice distortion through the introduction of large Al atoms into the CoCrFeNi matrix [3]. At the clad-substrate interface, a very sharp hardness transition was observed, consistent with its relatively small inter-diffusion thickness (i.e. ~30 μm).

After the isothermal holding treatment at 1000 °C, the thermally induced microstructural changes manifest in differing micro-hardness behavior (Fig. 10b). The $Al_{0.3}$ and $Al_{0.6}$ claddings maintained a similar hardness after isothermal holding to the as deposited condition, whereas there was significant softening in the $Al_{0.85}$ cladding with ~30% drop in micro-hardness after isothermal holding. This was accompanied by some fluctuation through the coating thickness, similar to that of $Al_{0.6}$ clad. Principally, the overall thermal softening ratio was in line with the magnitude of phase transformation though the isothermal holding treatment.

4. Discussion

In the current study, the $Al_xCoCrFeNi$ ($x = 0.3$, 0.6 and 0.85) single-layer HEA coatings were successfully produced, for the first time, by blown powder coaxial direct laser deposition (DLD) using selected parameters. The HEA coatings are mostly free of defects, homogenous in chemistry and controllable in dilution (~9%) with a very minimal inter-diffusion thickness of ~30 μm. The parametric studies reveal a strong dependence of cladding characteristics (e.g. powder efficiency and dilution) on the processing parameters. The as-deposited HEA coatings principally exhibit different simple solid solution structures depending on the Al ratio, despite the compositional variation induced by dilution. The HEA coatings produced here have different microstructural characteristics from the bulk HEAs produced by DLD or arc melting [35,46], most likely due to the distinct processing conditions.

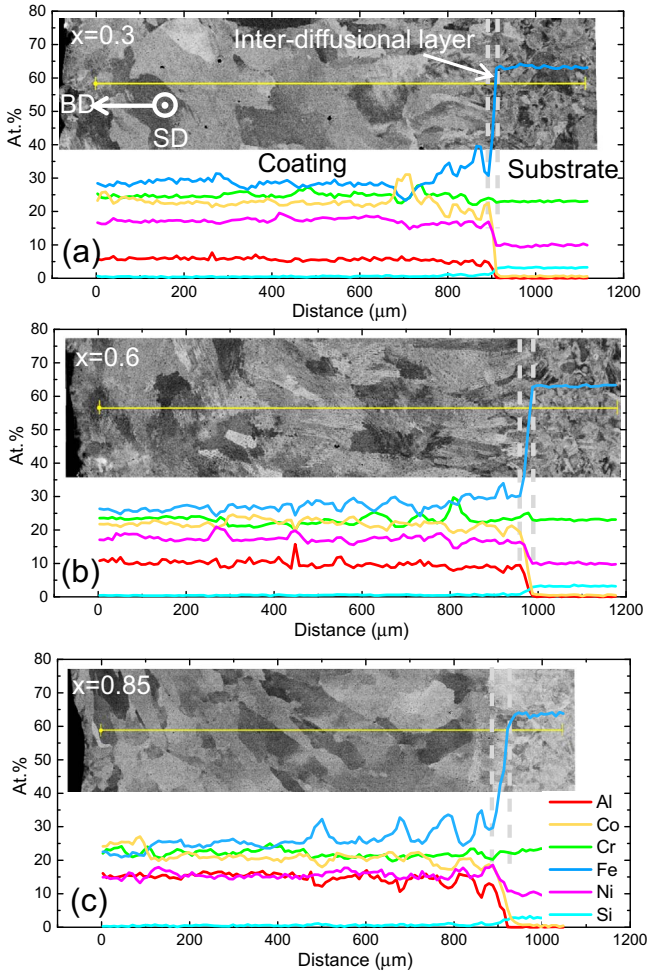

Fig. 6. SEM-EDS composition profile of the $Al_xCoCrFeNi$ coating depositions: a) $x = 0.3$, b) $x = 0.6$ and c) $x = 0.85$.

4.1. Effect of processing variables on clad efficiency

Compared with intensively studied powder bed approach of laser HEA cladding, the current blown powder coaxial DLD process represents a relatively lower powder efficiency (P_E = 9–38% for single-track deposits and 33–43% for single-layer claddings). This is because the powder is delivered coaxially by carrier gas to form a powder cloud under the laser beam in DLD, rather than a static pre-placed layer in the powder bed approach, and only part of the powder stream can be captured/melted by the laser beam to form a clad. To advance the application of DLD in HEA claddings, higher powder and energy efficiencies are desired from both economic and technical points of view. For a given laser cladding system, P_E is dependent on the combination of processing parameters (e.g. P, S, D, and F as shown in Fig. 3 and Table 1). Specifically, P_E is mainly proportional to laser power P, whereas the effect of other parameters (i.e. S, D, F) appears rather complex. Oliveira et al. [34] proposed a combined parameters $P\sqrt{F/S}$, which was believed to control P_E in coaxial DLD. However, no linear relationship between $P\sqrt{F/S}$ and P_E is found here (Fig. 13a), perhaps due to the relatively small data volume in the current study (i.e. deviation) or different strategies in the selection of processing parameters. In addition, the effect of laser beam size D on P_E is not counted in the combined parameter $P\sqrt{F/S}$, which may assert remarkable influence on the cladding efficiency by varying the energy density. For instance, a P_E of 30% was obtained at D = 2–3 mm (Figs. 2 and 3c), whereas no deposit was produced at a greater laser beam size of 4 mm when other parameters were maintained the same (Table 1).

In principle, the powder usage efficiency P_E is determined by the relative ratio between powder feeding rate (F) and specific energy density, as a successful cladding (e.g. HEA coating) on the substrate requires a minimum heat input to generate a melt pool consisting of both powder fillers and the substrate. The specific energy density (E_S) of a single laser track is given by [23],

$$E_S = [P/(\pi D^2/4)](D/S) = 4P/(\pi DS) \quad (3)$$

At a given powder feed rate, P_E principally follows an exponential relationship with E_S (e.g. dash line in Fig. 13a [39]): in the relatively low E_S region (i.e. 24–32 J·mm^{-2}), increasing E_S ($P\uparrow$, $D\downarrow$ or $S\downarrow$) generally leads to rapid enhancement in P_E (effective cladding); with further increase in E_S, there is no remarkable enhancement in P_E (e.g. when $P_E > 40$) but dilution and low energy efficiency can be caused. Further improvement in P_E can be potentially attained via reducing the powder delivery velocity in carrier gas, which is not addressed in the current study. An increase in the powder feeding rate F normally leads to greater cladding area A_C but not necessarily the same for powder efficiency P_E (Table 1 and Fig. 3d). This is because E_S may become insufficient for the high F condition to effectively melt a denser powder cloud under the laser beam (e.g. Fig. 3d).

The relatively low range of energy density used in the current study also resulted in the presence of pores and un-melted particles in the single laser tracks (Figs. 1 and 2), though their population was significantly reduced in multiple-track square depositions (Figs. 4a and 5). Indeed, the overall population of inclusions/pores in the current HEA cladding (Fig. 5) is still higher than that of bulk HEA columns manufactured in an earlier work [35] using similar parameters. This is mainly attributed to the accumulated higher energy density (Table 1) and heat transfer induced re-melting/annealing (normally in the range of many layers) during successive multiple-layer deposition of the latter bulk HEA columns.

4.2. Effect of processing variables on dilution

Dilution is almost inevitable in laser cladding as the powder fillers and substrate are partially intermixed in the melt pool created by the laser to form metallurgical bonding. However, a controlled dilution level is desired as dilution is detrimental to coating properties, including hardness, corrosion resistance [41] and HEA solid solution formability as will be discussed. In a DLD process, the extent of dilution and thickness of inter-diffusion layer are expected to increase by increasing the laser-material interaction time (D/S), specific energy input ($E_S = 4P/(\pi DS)$) and the relative ratio of laser energy taken by the

Table 2
The designed and measured HEA cladding compositions and corresponding parameters for predicting their solid solution formability.

HEA compositions		Al (at.%)	Co (at.%)	Cr (at.%)	Fe (at.%)	Ni (at.%)	Mn (at.%)	Si (at.%)	O (at.%)	F_C (%)	Ω	δ (%)	ΔH_{mix} (kJ/mol)
Calibrated elemental powders	$Al_{0.3}$	6.97	23.25	23.25	23.25	23.25	/	/	/	/	3.19	3.73	−7.26
	$Al_{0.6}$	13.04	21.74	21.74	21.74	21.74	/	/	/	/	2.35	4.88	−9.87
	$Al_{0.85}$	17.53	20.62	20.62	20.62	20.62	/	/	/	/	1.98	5.47	−11.52
Measured HEA coatings	$Al_{0.3}$	5.69	22.73	23.78	27.19	18.7	0.15	0.47	1.31	5.7	2.33	3.74	−7.89
	$Al_{0.6}$	10.23	21.88	22.39	25.93	17.3	0.15	0.43	1.37	6.3	1.94	4.85	−9.63
	$Al_{0.85}$	16.05	21.6	20.9	24.45	15.47	0.14	0.44	0.96	5.4	1.57	6.57	−11.59

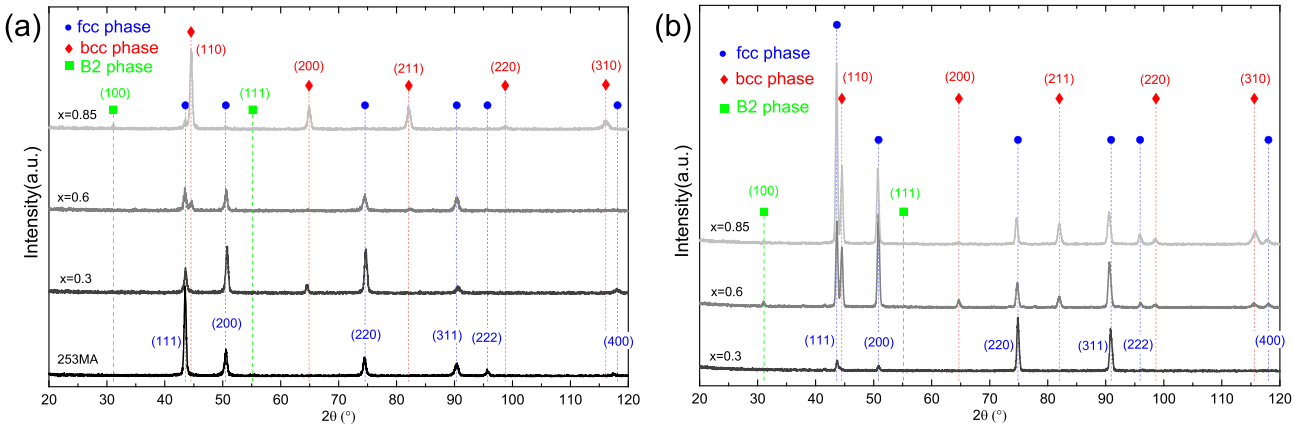

Fig. 7. XRD diffractograms of the $Al_xCoCrFeNi$ claddings a) before and b) after isothermal holding treatment at 1000 °C for 100 h.

substrate (P_{ms}) with respect to powder (P_{mp}). Specifically, dilution increases with increasing laser power P but typically decreases with laser scanning speed S (Fig. 3a, b). An increase in F results in a lower P_{mp}/P_{ms} ratio and hence diminishes dilution (Fig. 3d). Oliveira et al. [34] successfully combined the influence of these variables into a parameter $\sqrt{PS/F}$, which reasonably fits the current data (Fig. 13b). Still, there is some deviation as the effect of laser beam diameter D on dilution is not reflected in the combined parameter. In fact, enlarging D results in an increased laser-powder interaction time and reduced specific energy density. As the latter counts more in dilution, D is inversely proportional to F_D. Taking this into account, the combined parameter can be adopted into $\sqrt{PS/DF}$, yielding a much better liner fit with F_D (Fig. 13b). It should be noted that the extent of dilution and inter-diffusion thickness are relatively small in the current study, compared with many other HEA claddings produced by either blown powder [32] or powder bed [41] approaches. The successful control of dilution in the ~900 μm thick single-layer HEA cladding is mainly due to the unique combination of processing parameters, which largely reduces the later-material interaction time and specific energy density compared with prior studies. Further study will be oriented towards improving the coating properties without compromising dilution.

4.3. Rationalizing HEA cladding microstructures

In general, the overall phase constitution of the $Al_xCoCrFeNi$ (x = 0.3, 0.6 and 0.85) HEA claddings is comparable to that of the bulk samples produced by arc melting and DLD. The observed increase in the fraction of the Al-Ni-rich BCC phase with increasing Al content is also consistent with the literature studies [3,10,35]. However, the HEA coatings produced here displayed different microstructural characteristics from the bulk HEAs produced by DLD or arc melting. For instance, the Al-rich grain boundary segregation revealed by the bulk DLD $Al_{0.3}$

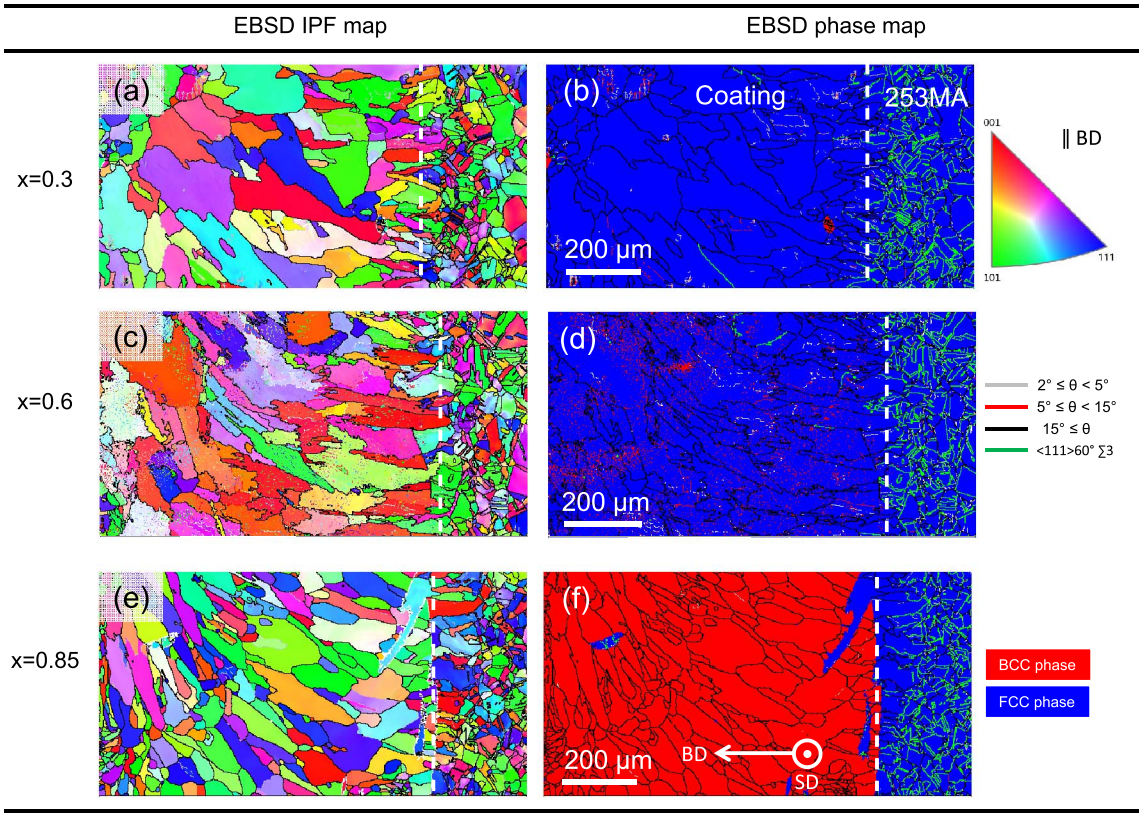

Fig. 8. EBSD IPF and phase maps of the $Al_xCoCrFeNi$ coating depositions: a–b) x = 0.3, c–d) x = 0.6, e–f) x = 0.85.

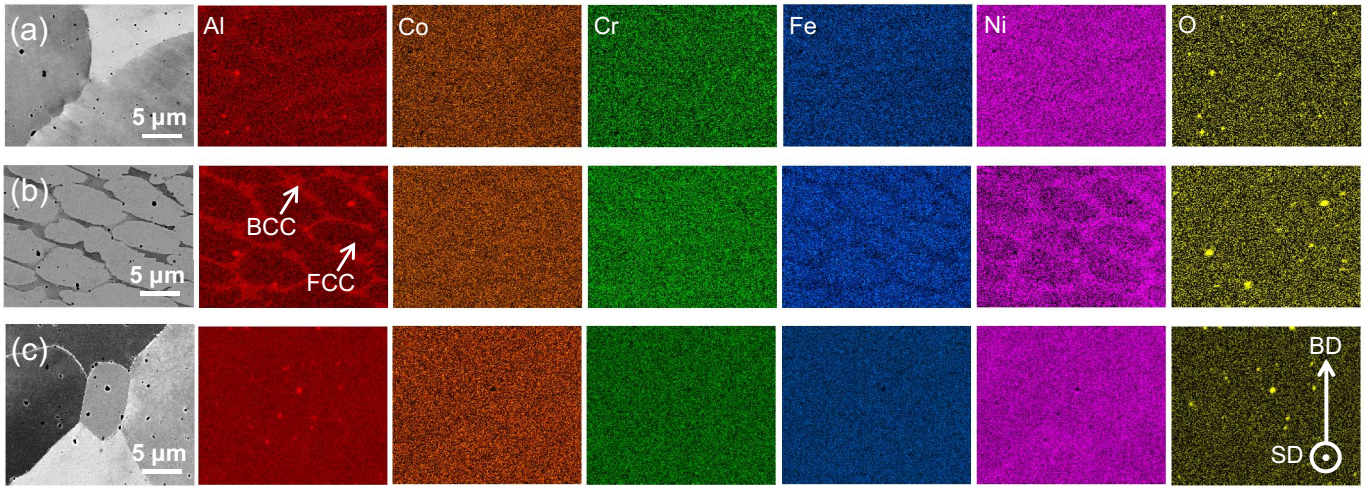

Fig. 9. EDS maps of the $Al_xCoCrFeNi$ coating depositions: a) $x = 0.3$, b) $x = 0.6$, c) $x = 0.85$.

HEA [34] was not observed in the HEA claddings, instead sub-structural cellular networks were found throughout the FCC grain interior. The $Al_{0.6}$ bulk HEAs manufactured by arc casting and DLD revealed an equiaxed Widmanstätten microstructure, whereas a dispersion of FCC phase in a matrix of columnar BCC grains was observed for the $Al_{0.6}$ HEA cladding. The $Al_{0.85}$ HEA cladding revealed some local grain boundary segregation, although the extent was reduced compared to bulk $Al_{0.85}$ HEA produced by DLD. Additionally, the disordered BCC matrix/ordered B2 cuboidal particle spinodal structure observed in arc melted and DLD bulk $Al_{0.85}$ HEA [35] did not occur in the cladding, where only the disordered BCC phase was observed. These microstructural differences are most likely attributed to the compositional variation induced by dilution and distinct processing conditions in DLD cladding.

As a result of dilution, the measured HEA composition in the as-deposited claddings is slightly altered from the designed ones (higher in Fe, but leaner in Al and Ni, Fig. 6 and Table 2). The effect of tuned Al ratio on the phase composition of the HEA claddings is schematically shown in an isopletic section of the $Al_xCoCrFeNi$ phase diagram calculated by Zhang et al. [47] using a database developed by CALPHAD approach (Fig. 14a), where all HEA clad compositions reveal a shift towards the low-Al FCC phase region. This is perhaps why no grain boundary segregation of Al rich phases is observed in the $Al_{0.3}$ HEA coating even after isothermal holding treatment. The compositional variation of the multicomponent HEA system can be quantified using a factor (F_C),

$$F_C = \sum_{i=1}^{i} \frac{(C_{Mi} - C_{Ni})^2}{(C_{Mi} + C_{Ni})/2} \quad (4)$$

where C_{Mi} and C_{Ni} represent the measured elemental fraction of the clad and nominal designed elemental fraction of the powder fillers (both in

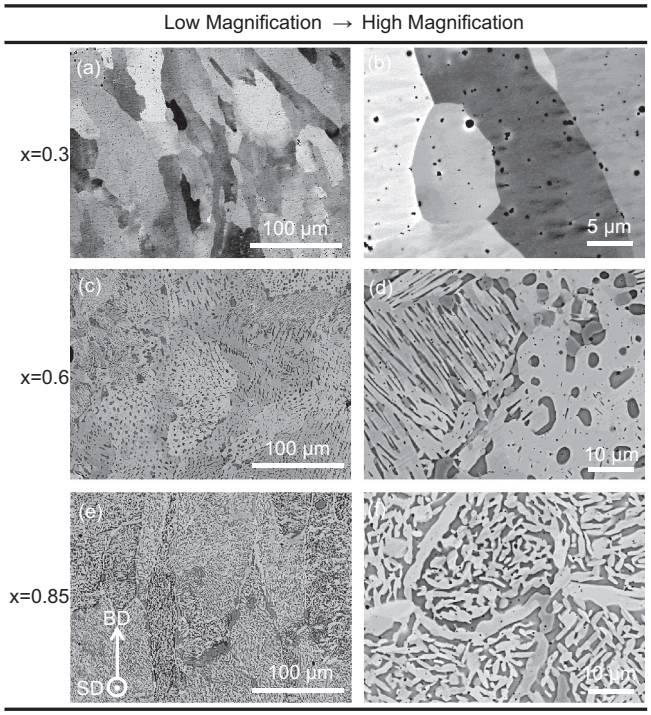

Fig. 11. Cross-sectional SEM micrographs of the $Al_xCoCrFeNi$ single layer coating depositions after isothermal holding at 1000 °C for 100 h: a–b) $x = 0.3$, c–d) $x = 0.6$, e–f) $x = 0.85$.

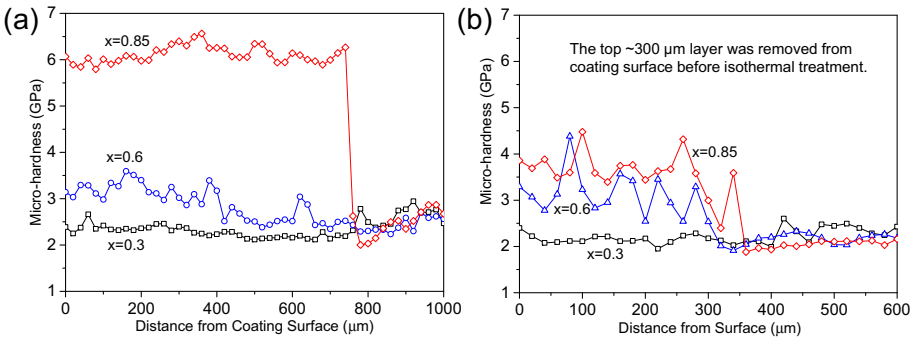

Fig. 10. Cross-sectional microhardness profile of the $Al_xCoCrFeNi$ claddings a) before and b) isothermal holding treatment at 1000 °C for 100 h.

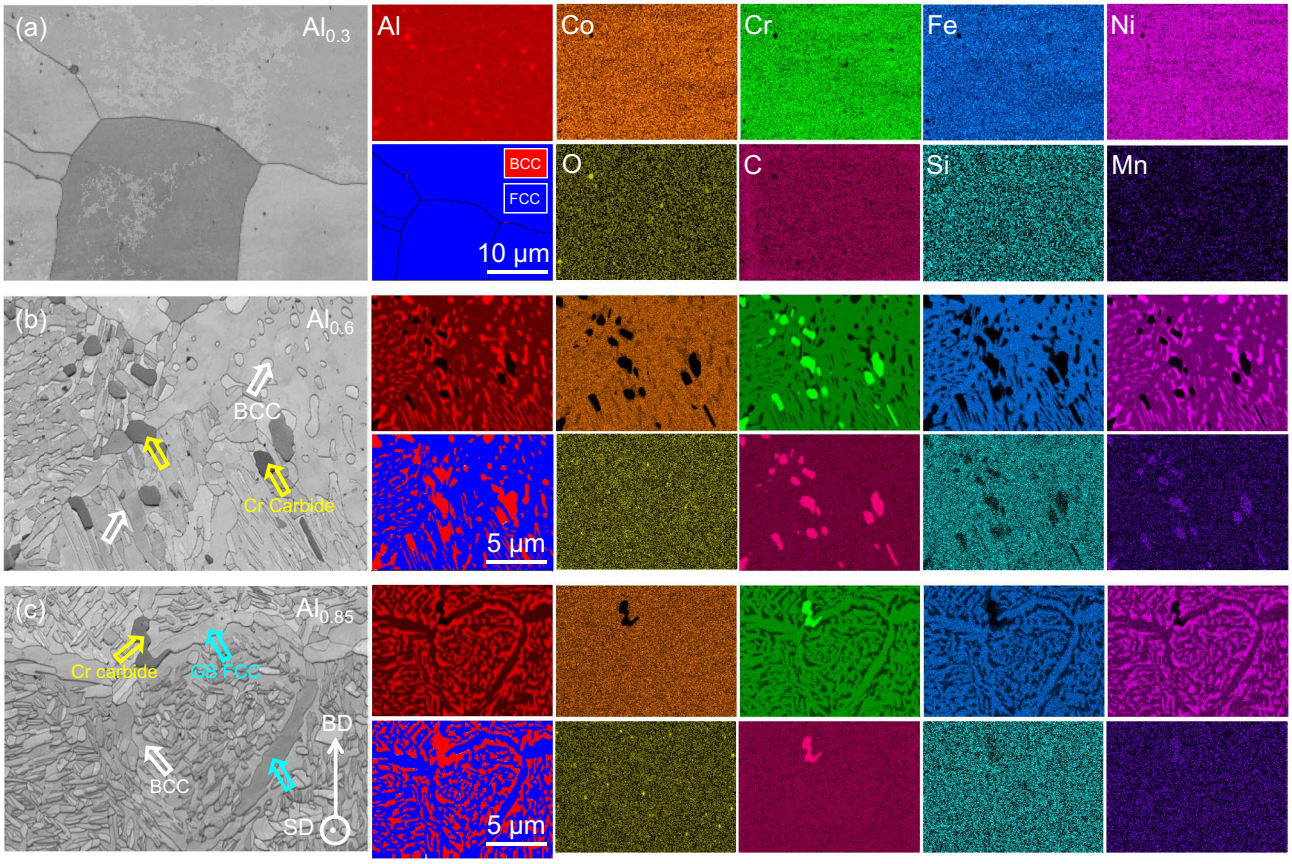

Fig. 12. Combined EBSD and EDS maps of the $Al_xCoCrFeNi$ coating depositions after isothermal holding treatment: a) x = 0.3, b) x = 0.6, c) x = 0.85.

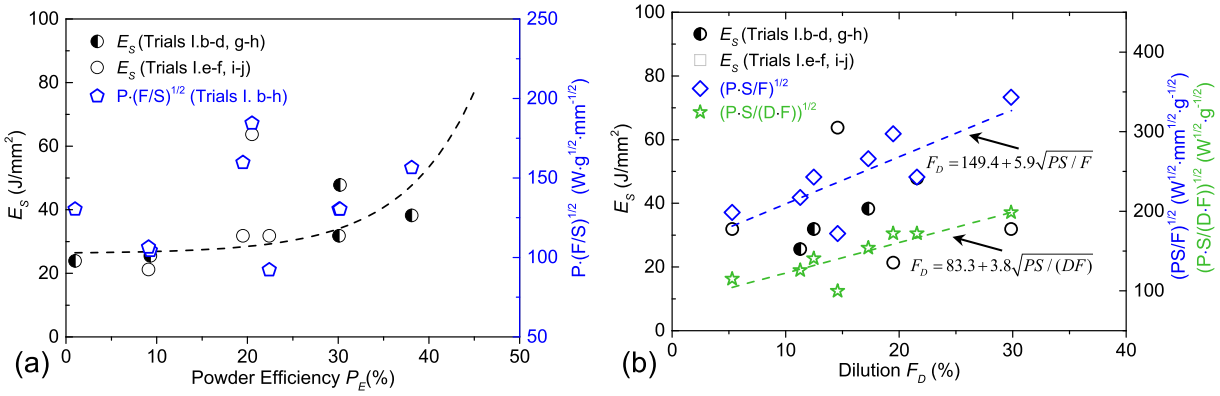

Fig. 13. The relationship between a) powder efficiency and b) dilution with specific energy density *Es* and combined parameters for the single-track depositions.

at.%), respectively. Here, a smaller F_C value denotes a lower level of dilution (F_C = 0 if no dilution). Compared to prior studies on blown powder DLD of HEA claddings ($F_C \approx$ 16%) [31,32], F_C is relatively low (5.4–6.3%) in the current study, consistent with the relatively low level of dilution. Nevertheless, the compositional deviation still results in a change in mixing entropies of the alloy system (ΔH_{mix}) and hence may affect their solid-solution stability. Based on a δ-Ω criteria proposed by Yang and Zhang [48], where δ is an atomic size parameter and Ω is a factor incorporating enthalpies and entropies of mixing and constituent melting points (a combination of δ < 6.6% and Ω > 1.1 for solid solution stability), the diluted HEA cladding compositions are less favorable for the formation of solid solutions (Table 2, Fig. 14). In particular, the $Al_{0.85}$ clad composition is very close to the solid solution boundary, outside of which undesirable brittle intermetallic phases are expected [6,48].

Due to the high thermal gradient and rapid solidification rate in DLD cladding [36,37], simple solid solution phases are obtained in the as deposited claddings, characteristic of unique non-equilibrium microstructures. For instance, thermal strain of the FCC $Al_{0.3}$ HEA coating with low stacking fault energy [33,49] may take place during the DLD process as a result of rapid solidification and a high thermal gradient, leading to the formation a dislocation networks throughout the microstructure. In addition, distinct from bulk HEA formation where the deposited zone is subjected to higher accumulated energy density and longer interaction time by successive layers, which in fact exposes the prior deposits to short time annealing, the time available for solute segregation and phase separation has been largely restricted in the single layer deposition. This is perhaps why the $Al_{0.6}$ bulk HEA appeared a Widmanstätten structure and more significant grain boundary segregation was observed in the $Al_{0.85}$ HEA.

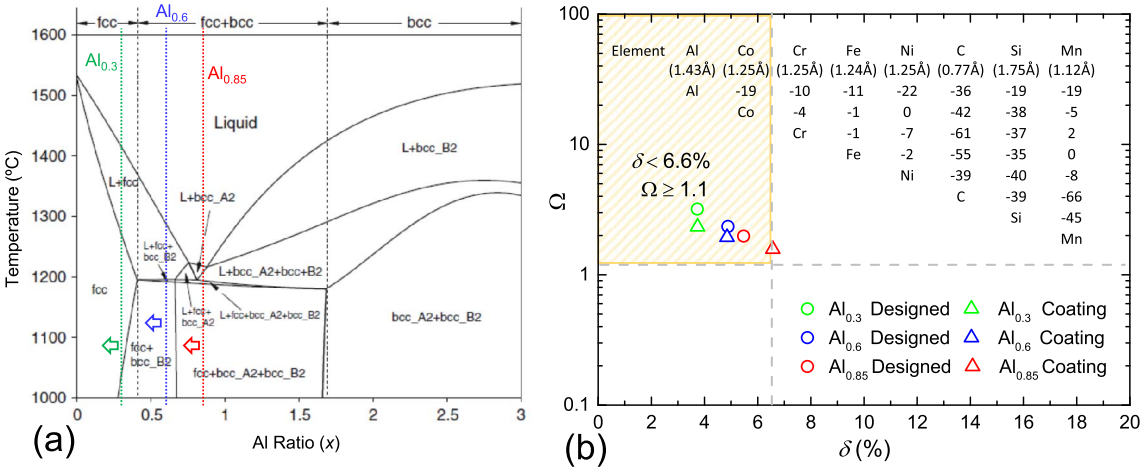

Fig. 14. a) Schematic representation of the dilution resultant composition variation in the HEA claddings using the equilibrium phase diagram of $Al_xCoCrFeNi$ system; b) prediction of solid solution formability in the HEAs using a δ-Ω criteria. The insert table is the atomic radius and the mixing enthalpy of atomic pairs for the elements in the HEA coatings (in kJ/mol).

The non-equilibrium microstructures produced by rapid solidification in the DLD cladding process experience distinct transformation towards the equilibrium phase composition during thermal exposure at 1000 °C for 100 h. The evolutions generally comprise the annihilation of the substructural cellular dislocation/segregation networks in the $Al_{0.3}$ HEA and different extent of phase separation in the $Al_{0.6}$ and $Al_{0.85}$ claddings. Depending on the extent of phase evolution (the replacement of hard BCC phase with softer B2 and FCC phases), the HEA claddings exhibits discrete thermal softening. Nevertheless, the $Al_{0.85}$ HEA coating retains relatively higher hardness than the substrate and other claddings after the isothermal heat treatment at 1000 °C for 100 h. In future HEA cladding, the effect of dilution on HEA cladding composition should be carefully considered, especially on microstructural changes and thermal stability. To expand knowledge on the potential of HEA claddings for high temperature applications, the evolution of microstructures and hardness over longer times and higher temperatures should be explored in subsequent research.

5. Conclusions

In the current work, the effect of key processing parameters on the deposition characteristics was studied through single track depositions of $Al_{0.3}CoCrFeNi$ on a 253MA steel plate, followed by single layer square cladding depositions. After that, the microstructure, mechanical property and thermal stability of $Al_xCoCrFeNi$ (x = 0.3, 0.6 and 0.85) single-layer HEA coatings were investigated. The following conclusions can be drawn from this work:

1) The dimensional characteristics of HEA laser cladding deposits were largely dependent on the processing variables. A linear relationship between dilution and a combined parameter $\sqrt{PS/(DF)}$ was found in the coaxial DLD processing.
2) Despite of slight compositional variation induced by dilution, simple solid solution structures were successfully produced in the single-layer $Al_xCoCrFeNi$ HEA coatings by blown powder DLD using selected parameters. The coatings were relatively chemically homogenous, defect-free and dilution-controllable with an inter-diffusion thickness of ~30 μm.
3) An increased Al mole fraction from 0.3 to 0.6 and 0.85 led to different crystal structures in the HEA coatings from FCC to duplex FCC + BCC and BCC, respectively. These coatings had unique microstructural characteristics such as substructural cellular networks, grain boundary/interphase segregation, which are quantitatively different from microstructures of the same alloys produced by DLD or arc melting.
4) The increased Al content resulted in increased microhardness in the as-deposited claddings and reduced microstructural stability upon isothermal treatment at 1000 °C and hence higher level of thermal softening.

Acknowledgments

The present work was carried out with the support of the Deakin Advanced Characterization Facility. The financial support by the Australian Research Council through the ARC Research Hub for Transforming Australia's Manufacturing Industry through High Value Additive Manufacturing (IH130100008) is gratefully acknowledged.

References

[1] J.W. Yeh, S.K. Chen, S.J. Lin, J.Y. Gan, T.S. Chin, T.T. Shun, C.H. Tsau, S.Y. Chang, Nanostructured high-entropy alloys with multiple principal elements: novel alloy design concepts and outcomes, Adv. Eng. Mater. 6 (5) (2004) 299–303.
[2] B. Cantor, I.T.H. Chang, P. Knight, A.J.B. Vincent, Microstructural development in equiatomic multicomponent alloys, Mater. Sci. Eng. A 375–377 (2004) 213–218.
[3] Y. Zhang, T.T. Zuo, Z. Tang, M.C. Gao, K.A. Dahmen, P.K. Liaw, Z.P. Lu, Microstructures and properties of high-entropy alloys, Prog. Mater. Sci. 61 (2014) 1–93.
[4] D.B. Miracle, O.N. Senkov, A critical review of high entropy alloys and related concepts, Acta Mater. 122 (2017) 448–511.
[5] B.S. Murty, J.W. Yeh, S. Ranganathan, High Entropy Alloys, Butterworth-Heinemann, Boston, 2014, pp. 133–148.
[6] Y.F. Ye, Q. Wang, J. Lu, C.T. Liu, Y. Yang, High-entropy alloy: challenges and prospects, Mater. Today 19 (6) (2016) 349–362.
[7] J.M. Wu, S.J. Lin, J.W. Yeh, S.K. Chen, Y.S. Huang, H.C. Chen, Adhesive wear behavior of $Al_xCoCrCuFeNi$ high-entropy alloys as a function of aluminum content, Wear 261 (5–6) (2006) 513–519.
[8] C.P. Lee, C.C. Chang, Y.Y. Chen, J.W. Yeh, H.C. Shih, Effect of the aluminium content of AlxCrFe1.5MnNi0.5 high-entropy alloys on the corrosion behaviour in aqueous environments, Corros. Sci. 50 (7) (2008) 2053–2060.
[9] K. Zhang, Z. Fu, Effects of annealing treatment on phase composition and microstructure of $CoCrFeNiTiAl_x$ high-entropy alloys, Intermetallics 22 (2012) 24–32.
[10] W.R. Wang, W.L. Wang, J.W. Yeh, Phases, microstructure and mechanical properties of AlxCoCrFeNi high-entropy alloys at elevated temperatures, J. Alloys Compd. 589 (2014) 143–152.
[11] S. Singh, N. Wanderka, B.S. Murty, U. Glatzel, J. Banhart, Decomposition in multi-component AlCoCrCuFeNi high-entropy alloy, Acta Mater. 59 (1) (2011) 182–190.
[12] T.M. Butler, M.L. Weaver, Investigation of the phase stabilities in AlNiCoCrFe high entropy alloys, J. Alloys Compd. 691 (2017) 119–129.
[13] K.Y. Tsai, M.H. Tsai, J.W. Yeh, Sluggish diffusion in Co–Cr–Fe–Mn–Ni high-entropy alloys, Acta Mater. 61 (13) (2013) 4887–4897.
[14] C. Huang, Y. Zhang, J. Shen, R. Vilar, Thermal stability and oxidation resistance of laser clad TiVCrAlSi high entropy alloy coatings on Ti–6Al–4V alloy, Surf. Coat. Technol. 206 (6) (2011) 1389–1395.
[15] T.M. Butler, J.P. Alfano, R.L. Martens, M.L. Weaver, High-temperature oxidation behavior of Al-Co-Cr-Ni-(Fe or Si) multicomponent high-entropy alloys, JOM 67 (1) (2015) 246–259.
[16] G.R. Holcomb, J. Tylczak, C. Carney, Oxidation of CoCrFeMnNi high entropy alloys, JOM 67 (10) (2015) 2326–2339.

[17] G. Laplanche, U.F. Volkert, G. Eggeler, E.P. George, Oxidation behavior of the CrMnFeCoNi high-entropy alloy, Oxid. Met. 85 (5–6) (2016) 629–645.
[18] W.Y. Huo, H.F. Shi, X. Ren, J.Y. Zhang, Microstructure and wear behavior of CoCrFeMnNbNi high-entropy alloy coating by TIG cladding, Adv. Mater. Sci. Eng. 2015 (2015) 5.
[19] T.K. Chen, T.T. Shun, J.W. Yeh, M.S. Wong, Nanostructured nitride films of multi-element high-entropy alloys by reactive DC sputtering, Surf. Coat. Technol. 188–189 (2004) 193–200.
[20] W.L. Hsu, H. Murakami, J.W. Yeh, A.C. Yeh, K. Shimoda, On the study of thermal-sprayed Ni0.2Co0.6Fe0.2CrSi0.2AlTi0.2 HEA overlay coating, Surf. Coat. Technol. 316 (2017) 71–74.
[21] C. Zhang, G.J. Chen, P.Q. Dai, Evolution of the microstructure and properties of laser-clad FeCrNiCoB$_x$ high-entropy alloy coatings, Mater. Sci. Technol. 32 (16) (2016) 1666–1672.
[22] M. Zhang, X. Zhou, X. Yu, J. Li, Synthesis and characterization of refractory TiZrNbWMo high-entropy alloy coating by laser cladding, Surf. Coat. Technol. 311 (2017) 321–329.
[23] S. Zhang, C.L. Wu, C.H. Zhang, M. Guan, J.Z. Tan, Laser surface alloying of FeCoCrAlNi high-entropy alloy on 304 stainless steel to enhance corrosion and cavitation erosion resistance, Opt. Laser Technol. 84 (2016) 23–31.
[24] S. Zhang, C.L. Wu, J.Z. Yi, C.H. Zhang, Synthesis and characterization of FeCoCrAlCu high-entropy alloy coating by laser surface alloying, Surf. Coat. Technol. 262 (2015) 64–69.
[25] X. Ye, M. Ma, Y. Cao, W. Liu, X. Ye, Y. Gu, The property research on high-entropy alloy Al$_x$FeCoNiCuCr coating by laser cladding, Phys. Procedia 12 (2011) 303–312.
[26] H. Zhang, Y. Pan, Y.Z. He, Synthesis and characterization of FeCoNiCrCu high-entropy alloy coating by laser cladding, Mater. Des. 32 (4) (2011) 1910–1915.
[27] H. Zhang, Y. Pan, Y. He, H. Jiao, Microstructure and properties of 6FeNiCoSiCrAlTi high-entropy alloy coating prepared by laser cladding, Appl. Surf. Sci. 257 (6) (2011) 2259–2263.
[28] C.L. Wu, S. Zhang, C.H. Zhang, J. Chen, S.Y. Dong, Phase evolution characteristics and corrosion behavior of FeCoCrAlCu-X$_{0.5}$ coatings on cp Cu by laser high-entropy alloying, Opt. Laser Technol. 94 (2017) 68–71.
[29] C.L. Wu, S. Zhang, C.H. Zhang, H. Zhang, S.Y. Dong, Phase evolution and properties in laser surface alloying of FeCoCrAlCuNi$_x$ high-entropy alloy on copper substrate, Surf. Coat. Technol. 315 (2017) 368–376.
[30] Y. Shon, S.S. Joshi, S. Katakam, R. Shanker Rajamure, N.B. Dahotre, Laser additive synthesis of high entropy alloy coating on aluminum: corrosion behavior, Mater. Lett. 142 (2015) 122–125.
[31] T.M. Yue, H. Xie, X. Lin, H.O. Yang, G.H. Meng, Solidification behaviour in laser cladding of AlCoCrCuFeNi high-entropy alloy on magnesium substrates, J. Alloys Compd. 587 (2014) 588–593.
[32] V. Ocelík, N. Janssen, S.N. Smith, J.T.M. De Hosson, Additive manufacturing of high-entropy alloys by laser processing, JOM 68 (7) (2016) 1810–1818.
[33] H. Zhang, Y.-Z. He, Y. Pan, S. Guo, Thermally stable laser cladded CoCrCuFeNi high-entropy alloy coating with low stacking fault energy, J. Alloys Compd. 600 (2014) 210–214.
[34] U. de Oliveira, V. Ocelík, J.T.M. De Hosson, Analysis of coaxial laser cladding processing conditions, Surf. Coat. Technol. 197 (2–3) (2005) 127–136.
[35] J. Joseph, T. Jarvis, X. Wu, N. Stanford, P. Hodgson, D.M. Fabijanic, Comparative study of the microstructures and mechanical properties of direct laser fabricated and arc-melted AlxCoCrFeNi high entropy alloys, Mater. Sci. Eng. A 633 (2015) 184–193.
[36] K.I. Schwendner, R. Banerjee, P.C. Collins, C.A. Brice, H.L. Fraser, Direct laser deposition of alloys from elemental powder blends, Scr. Mater. 45 (10) (2001) 1123–1129.
[37] L. Thijs, K. Kempen, J.P. Kruth, J. Van Humbeeck, Fine-structured aluminium products with controllable texture by selective laser melting of pre-alloyed AlSi10Mg powder, Acta Mater. 61 (5) (2013) 1809–1819.
[38] Z.G. Yang, D.M. Paxton, K.S. Weil, J.W. Stevenson, P. Singh, Materials properties database for selection of high-temperature alloys and concepts of alloy design for SOFC applications, Pacific Northwest National Laboratory (PNNL), Richland, WA (US), 2002.
[39] G.J. Bruck, Fundamentals and industrial applications of high power laser beam cladding, SPIE Proc. Laser Beam Surf. Treating Coat. 957 (1988) 14–28.
[40] V. Ocelík, O. Nenadl, A. Palavra, J.T.M. De Hosson, On the geometry of coating layers formed by overlap, Surf. Coat. Technol. 242 (2014) 54–61.
[41] I. Hemmati, V. Ocelík, J.T.M. De Hosson, Dilution effects in laser cladding of Ni–Cr–B–Si–C hardfacing alloys, Mater. Lett. 84 (2012) 69–72.
[42] A. Rukwied, A.W. Ruff, W.A. Willard, Study of the cellular solidification structure in a continuously cast high purity copper, Metall. Mater. Trans. B Process Metall. Mater. Process. Sci. 2 (8) (1971) 2105–2114.
[43] K. Saeidi, X. Gao, Y. Zhong, Z.J. Shen, Hardened austenite steel with columnar subgrain structure formed by laser melting, Mater. Sci. Eng. A 625 (2015) 221–229.
[44] J.C. Rao, V. Ocelík, D. Vainchtein, Z. Tang, P.K. Liaw, J.T.M. De Hosson, The fcc-bcc crystallographic orientation relationship in AlxCoCrFeNi high-entropy alloys, Mater. Lett. 176 (2016) 29–32.
[45] J. Joseph, N. Stanford, P. Hodgson, D.M. Fabijanic, Tension/compression asymmetry in additive manufactured face centered cubic high entropy alloy, Scr. Mater. 129 (2017) 30–34.
[46] Y.F. Kao, T.J. Chen, S.K. Chen, J.W. Yeh, Microstructure and mechanical property of as-cast, -homogenized, and -deformed AlxCoCrFeNi ($0 \le x \le 2$) high-entropy alloys, J. Alloys Compd. 488 (2009) 57–64.
[47] C. Zhang, F. Zhang, S. Chen, W. Cao, Computational thermodynamics aided high-entropy alloy design, JOM 64 (2012) 839–845.
[48] X. Yang, Y. Zhang, Prediction of high-entropy stabilized solid-solution in multi-component alloys, Mater. Chem. Phys. 132 (2–3) (2012) 233–238.
[49] Z. Li, S. Zhao, H. Diao, P.K. Liaw, M.A. Meyers, High-velocity deformation of Al (0.3)CoCrFeNi high-entropy alloy: remarkable resistance to shear failure, Sci. Rep. 7 (2017) 42742.